RSC Advances

PAPER

View Article Online
View Journal | View Issue

Cite this: *RSC Adv.*, 2024, **14**, 22569

pH-Dependent selective extraction of gold(III) from synthetic solution and computer motherboard leachate using a hybrid nanocomposite†

Rabeea D. Abdel-Rahim, Mahmoud Thabet, Ahmed R. Abdellah, Mohamed O. Saleh, Ahmed M. M. Fadl, Adham M. Nagiub and Hassanien Gomaa *

Received 19th June 2024
Accepted 10th July 2024

DOI: 10.1039/d4ra04476b

rsc.li/rsc-advances

Recycling gold from electronic waste offers significant benefits for both environmental protection and resource sustainability. However, this process presents considerable challenges due to high costs, prolonged processing times, and interference from coexisting metals. In this study, we synthesized a hybrid mesoporous nanocomposite comprising platelets-like $CoNi_2S_4$ incorporated with g-C_3N_4 nanosheets ($CoNi_2S_4$@g-C_3N_4) for the selective recovery of gold (Au(III)) ions from spent computer motherboards. Comprehensive characterization of the $CoNi_2S_4$@g-C_3N_4 nanocomposite was conducted, including its physicochemical properties, textural and structural characteristics, morphology, and elemental composition. The $CoNi_2S_4$@g-C_3N_4 extractor demonstrated an exceptional adsorption capacity of 200.6 mg g^{-1}, with high selectivity at pH 2, rapid equilibrium time of 60 minutes, and satisfactory reusability for over ten cycles. Adsorption isotherm and kinetic studies revealed that the $CoNi_2S_4$@g-C_3N_4 nanocomposite adheres to the Langmuir adsorption model and the pseudo-second-order kinetic model for Au(III) ion adsorption. Overall, this study introduces a viable adsorbent that shows considerable promise for industrial-scale Au(III) extraction from e-waste.

1. Introduction

Electronic waste (e-waste) represents a rapidly expanding solid waste stream, projected to reach 61.3 million tons annually by 2023.[1,2] Unlike conventional solid wastes, e-waste contains a unique combination of hazardous and resource-rich materials, with only 17.4% currently being effectively recovered due to underdeveloped technologies.[3–5] Spent motherboards (SMBs) from obsolete computers are a significant category of e-waste, containing valuable base metals (*e.g.*, copper, lead, tin) and precious metals (*e.g.*, gold, silver, palladium).[6] Among these, gold (Au) is particularly valuable due to its extensive use in electronics, telecommunications, aerospace, and other high-tech industries.[7–10] Efficient recovery of Au(III) ions from SMBs is crucial for sustainable resource utilization and environmental protection.[11,12] Therefore, efficient and sustainable technologies for Au(III) recovery from SMBs must be designed.

Methods for Au(III) recovery from e-waste involve pyrometallurgy and hydrometallurgy. A pyrometallurgical method often involves directly burning e-waste, which can produce by-pollutants and harmful materials. In contrast, the hydrometallurgical method provides a more environmentally friendly approach by utilizing digestive liquids to dissolve e-waste components before recovering the aimed species. The obtained solution undergoes subsequent extraction and purification processes.[13,14] Various gold extraction technologies, such as ion exchange, precipitation, flotation, solvent extraction, and adsorption, have been developed.[15] However, many of these approaches have noteworthy drawbacks, including high reagent requirements, the use of poisonous chemicals, and the production of toxic by-waste that necessitates discarding.[16,17] Among these methods, adsorption stands out as the most reliable technique for gold extraction due to its low cost, simplicity, efficiency, and reusability.[18,19] Recent developments have led to the creation of various adsorbents for trapping Au(III) ions, including biomass materials,[20] ion imprinting polymers,[21,22] carbon-based materials,[23] and metal–organic frameworks.[21] However, many of these adsorbents suffer from limitations such as lower adsorption capacities, slower kinetics, and reduced selectivity in the presence of competing ions. In this manuscript, we aim to design a stable adsorbent with a high adsorption capacity and selectivity feature for Au(III)-recovery from e-waste, even in the existence of other competing ions.

In recent years, graphitic carbon nitride (g-C_3N_4) has gained significant attention due to its unique physicochemical properties, including high chemical stability, higher electronic characteristics, plentiful functional groups, efficient visible light

Department of Chemistry, Faculty of Science, Al-Azhar University, Assiut 71524, Egypt. E-mail: h.gomaa@azhar.edu.eg

† Electronic supplementary information (ESI) available. See DOI: https://doi.org/10.1039/d4ra04476b

absorption for photocatalytic reactions, and acceptable adsorption capacity.[22–24] In addition, g-C_3N_4 has plenty of π-conjugated electrons and nitrogen-containing active sites, enabling the formation of covalent bonds with cations such as Au(III) ions. Despite these advantages, g-C_3N_4's adsorption performance is often limited by its relatively low surface area and restricted pore structure. Various strategies have been employed to enhance g-C_3N_4's adsorption properties, including texture modification, elemental manipulation, and incorporation with other materials.[25] Introducing metal sulfides, particularly binary metal sulfides such as $CoNi_2S_4$, offers a promising approach to enhance the adsorption performance of g-C_3N_4. Metal sulfides exhibit improved surface morphology, electrical conductivity, thermal stability, and diverse redox properties, leading to efficient Au(III) trapping.[26,27] Binary metal sulfide compounds exhibit superior performance compared to single metal sulfides.[28,29] However, to the best of our knowledge, the direct incorporation of $CoNi_2S_4$ into the g-C_3N_4 matrix to trap and extract Au(III) ions from e-waste has not been previously reported.

This study introduces a selective recovery method for Au(III) ions from e-waste-derived SMBs utilizing a mesoporous $CoNi_2S_4$@g-C_3N_4 nanocomposite. We comprehensively evaluated the Au(III) adsorption properties of the $CoNi_2S_4$@g-C_3N_4 nanocomposite compared to the original g-C_3N_4. The report encompasses four main aspects: (i) synthesis and detailed characterization of g-C_3N_4 and $CoNi_2S_4$@g-C_3N_4 nanocomposites, (ii) investigation of the Au(III) adsorption properties of g-C_3N_4 and $CoNi_2S_4$@g-C_3N_4 adsorbents, considering variables such as solution pH, contact time, sorbent dosage, Au(III) concentration, and the presence of interfering ions typically found in e-waste leachates, (iii) assessment of the materials for Au(III) recovery from actual SMB leachate, demonstrating their practical utility, and (iv) discussion on the Au(III) adsorption mechanisms using isotherm and kinetic models to understand the adsorbents-Au(III) interaction. Our findings indicate that the mesoporous $CoNi_2S_4$@g-C_3N_4 extractor shows considerable promise for selectively extracting gold from SMBs. This innovative approach not only enhances the efficiency of the recovery process but also contributes to the development of sustainable technologies for resource utilization and environmental protection.

2. Experimental work

2.1. g-C_3N_4 synthesis

g-C_3N_4 was synthesized through a method involving the equal proportion mixing of urea and thiourea, followed by thorough grinding. A mixture of 10 g of urea and 10 g of thiourea was thoroughly ground and placed in a covered porcelain crucible. The crucible was then calcined at 600 °C for 3 hours in a muffle furnace under a nitrogen atmosphere. The resulting yellow g-C_3N_4 product was washed with deionized water and dried at 90 °C for 12 hours. The yield was approximately 35% (Fig. 1A).

2.2. Synthesis of $CoNi_2S_4$@g-C_3N_4

The $CoNi_2S_4$@g-C_3N_4 composite was fabricated through a multi-step process (Fig. 1B). Initially, polyvinylpyrrolidone (PVP, M wt 55 000 g mol^{-1}) weighing 0.5 grams was dissolved in 40 mL of deionized water under continuous stirring. To this solution, 2.18 grams of $Co(C_2H_3O_2)_2 \cdot 4H_2O$ was added, followed by a stirring period of 30 minutes. Subsequently, 1.52 grams of thiourea was incorporated into the mixture, which was then followed by the addition of 2.48 grams of $Ni(C_2H_3O_2)_2 \cdot 4H_2O$. The obtained solution was stirred for a further 30 minutes. Thereafter, 0.5 grams of pre-synthesized g-C_3N_4 was introduced to the solution and homogenized using ultrasonic agitation for a duration of 60 minutes. The homogenized mixture was then moved to a sealed autoclave for hydrothermal treatment at a temperature of 180 °C for 24 hours. The resulting black precipitate was isolated and thoroughly cleaned with deionized water three times to eliminate impurities. The final $CoNi_2S_4$@g-C_3N_4 product was obtained after drying at 75 °C overnight and was subsequently utilized for Au(III) adsorption experiments. The yield of $CoNi_2S_4$@g-C_3N_4 was approximately 82% based on the total weight of g-C_3N_4 and metal precursors used.

2.3. Au(III) adsorption methodology

A series of batch trials were performed to investigate the adsorption capacity of Au(III) onto g-C_3N_4 and $CoNi_2S_4$@g-C_3N_4. These experiments involved stirring 25 mL of a 30 ppm Au(III) solution with varying amounts of the adsorbent materials at

Fig. 1 Schematic design for g-C_3N_4 (A) and $CoNi_2S_4$@g-C_3N_4 synthesis (B).

room temperature, with the pH adjusted to a specific value. Small amounts of 0.1 M HCl or NaOH solutions were added as micro-drops to alter the pH of solutions. Following the stirring process, the samples were filtered, and the remaining Au(III) concentrations were measured using Atomic Absorption Spectroscopy. To construct adsorption isotherms, 20 mg of the adsorbents were added to 25 mL of an Au(III) solution of known concentration and stirred for 60 minutes at a pH of 2.0. Additionally, the influence of contact time on adsorption efficiency was assessed by introducing 20 mg of the adsorbent into 25 mL of a 30 ppm Au(III) solution, maintaining the temperature and pH at room conditions and 2.0, respectively, and conducting periodic analyses. The adsorption performance of g-C_3N_4 and $CoNi_2S_4$@g-C_3N_4 and the Au(III)-adsorbed amount (q_e, mg g^{-1}) were calculated by determining the difference in concentration before and after the adsorption process, using the following equations:[30,31]

$$\text{Ads. } \% = \frac{C_o - C_e}{C_o} \times 100$$

$$q_e = (C_o - C_e) \times V/m$$

C_o and C_e (ppm) represent the original and final concentrations of Au(III), respectively. The dose of the g-C_3N_4 and $CoNi_2S_4$@g-C_3N_4 adsorbents is denoted as m (g), and V (L) refers to the Au(III) solution volume. The adsorbed Au(III) ions could be released/eluted using an eluent agent, such as NaOH combined with thiourea, through a batch protocol. The elution proficiency was calculated using the next equation:[32,33]

$$\text{Elution } \% = C_r/C_a \times 100$$

C_r and C_a (ppm) represent the concentrations of released and adsorbed Au(III) ions, respectively. The recycled g-C_3N_4 and $CoNi_2S_4$@g-C_3N_4 adsorbents were reused for up to 10 adsorption–elution cycles using a batch design. The practical applicability of g-C_3N_4 and $CoNi_2S_4$@g-C_3N_4 adsorbents was tested by extracting Au(III) ions from the leach liquor of e-waste. Each experiment was performed in triplicate and repeated thrice to guarantee reproducibility.

3. Outcomes and discussion

3.1. Adsorbents characterization

To investigate the morphology and microstructure of the g-C_3N_4 sample, scanning electron microscopy (SEM) images (Fig. 2A) reveal a nanosheet-like morphology, with these sheets assembling into large blocks approximately 30 μm in size. Transmission electron microscopy (TEM) images (Fig. 2B) show g-C_3N_4 nanosheets with widths and lengths ranging from 50 to 100 nm and ultrathin thicknesses. Darker regions in the TEM images indicate the overlap of several few-layer g-C_3N_4 sheets, enhancing the diffusion and trapping performance of Au(III) ions. High-resolution TEM (HRTEM) images (Fig. 2C) of g-C_3N_4 reveal uniformly distributed lattice fringe distances of 0.21 nm corresponding to the (002) plane. Selected area electron diffraction (SAED) patterns (Fig. 2D) show two concentric rings, confirming the crystal structure and corresponding to the (100) and (002) planes of g-C_3N_4. The morphology of the $CoNi_2S_4$@g-C_3N_4 sample was examined using SEM and TEM (Fig. 2E–H). SEM images (Fig. 2E and F) display platelets-like $CoNi_2S_4$ incorporated with g-C_3N_4 nanosheets. TEM images (Fig. 2G and H) illustrate the grafting of $CoNi_2S_4$ platelets among the sheet-like surfaces of g-C_3N_4. HRTEM analysis (Fig. 2I) indicates cubic $CoNi_2S_4$ planes and g-C_3N_4, with inter-planar spacings of 0.3 nm, 0.25 nm, and 0.28 nm corresponding to the (311), (400), and (440) crystal planes of $CoNi_2S_4$ nanoparticles, respectively. SAED patterns (Fig. 2J) further confirm the successful formation of the $CoNi_2S_4$@g-C_3N_4 nanocomposite by showing several diffraction rings that correspond to the lattice planes of both $CoNi_2S_4$ crystal and g-C_3N_4. Mapping of ingredients and energy-dispersive X-ray spectroscopy (EDS) profiles of g-C_3N_4 (Fig. 2K and S1†) demonstrate the homogenous distribution of C, N, and S elements throughout the surface. The atomic percentages of C, N, and S are 39.58%, 56.41%, and 4.01%, respectively, with the presence of sulfur attributed to the use of thiourea during synthesis. Elemental mapping images (Fig. 2L) of $CoNi_2S_4$@g-C_3N_4 show a homogeneous distribution of C, N, Co, Ni, and S elements, with atomic percentages of 24.68%, 38.6%, 9.45%, 6.83%, and 20.44%, respectively. In summary, these results confirm the successful formation of the $CoNi_2S_4$@g-C_3N_4 nanocomposite.

The X-ray diffraction (XRD) patterns depicted in Fig. 3A were utilized for phase analysis of g-C_3N_4, $CoNi_2S_4$, and $CoNi_2S_4$@g-C_3N_4. The observed XRD peaks are consistent with the g-C_3N_4 phase (JCPDS 87–1526). Specifically, the notable peak at 27.45° typically assigned to the (002) plane of graphitic materials, while a minor diffraction peak at 12.54° corresponds to an interplanar (100) plane.[34] Distinct peaks attributed to $CoNi_2S_4$ are observed at 16.2°, 26.36°, 31.5°, 37.9°, 49.8°, and 54.67°, which align well with the (111), (220), (311), (400), (511), and (440) facets of the cubic phase $CoNi_2S_4$ structure, as per standard pattern JCPDS no. 24-0334.[26,35] Furthermore, the XRD pattern of the $CoNi_2S_4$@g-C_3N_4 composite exhibits integrated peaks from both g-C_3N_4 and $CoNi_2S_4$, confirming the successful creation of the $CoNi_2S_4$@g-C_3N_4 nanocomposite.

X-ray photoelectron spectroscopy (XPS) was utilized to investigate the chemical bonding, chemical composition, and valence states of elemental components. The XPS survey spectra indicated the presence of C, N, O, and trace amounts of S in the g-C_3N_4 sample (Fig. S2A†). The origin of the oxygen and sulfur is likely from the urea and thiourea used in the synthesis process. High-resolution XPS spectra for the C 1s and N 1s regions of g-C_3N_4 showed distinct peaks at binding energies (BE) of 284.77 eV and 288.25 eV, which correspond to sp^2 C–C and N–C=N bonding, respectively (Fig. S2B†). The N 1s spectrum exhibited peaks at BEs of 398.79 eV and 401.1 eV, characteristic of C–N–H and C–N=N bonds, respectively (Fig. S2C†). These spectral features are consistent with those of pure g-C_3N_4, thereby confirming the successful synthesis of g-C_3N_4.[36,37] For the $CoNi_2S_4$@g-C_3N_4 sample, the C 1s spectrum exhibits peaks at BE of 289.25 eV and 284.75 eV, while the N 1s spectrum

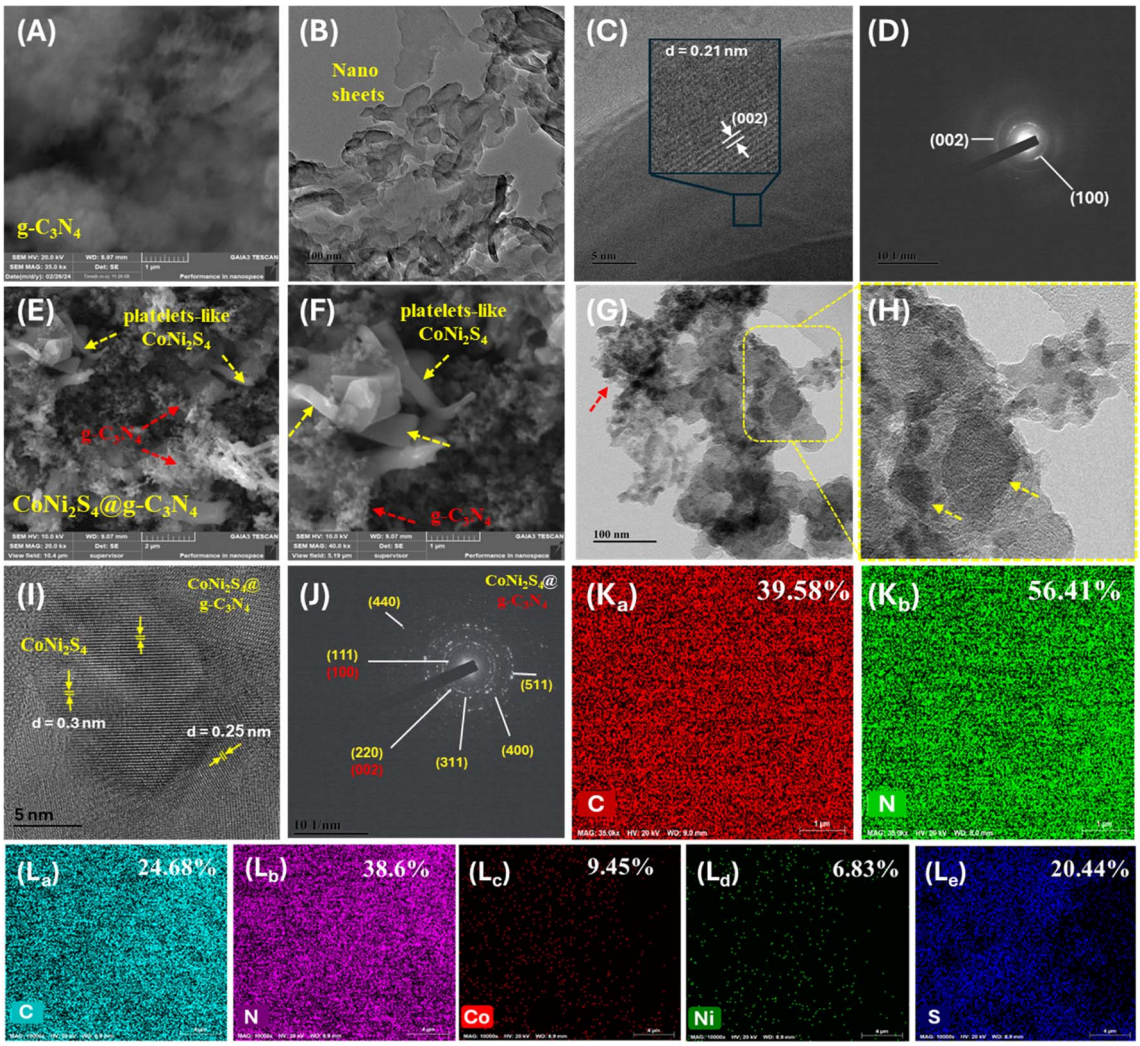

Fig. 2 SEM (A), TEM (B), HRTEM (C), and SAED images (D) of the g-C_3N_4 sample; SEM (E and F), TEM (G and H), HRTEM (I), SAED images (J) of $CoNi_2S_4$@g-C_3N_4; elemental mapping of g-C_3N_4 (K_{a-b}) and $FeNi_2S_4$@g-C_3N_4 (L_{a-e}) samples.

displays peaks at BE of 400.3 eV (Fig. 3B and C). Some shifts in BE values are observed, likely due to the grafting of $CoNi_2S_4$ onto the g-C_3N_4 surface. In the Co 2p XPS spectrum (Fig. 3D), the peaks at 778.8 and 793.8 eV for Co $2p_{3/2}$ and Co $2p_{1/2}$ are characteristic peaks of Co^{3+}. While the remaining peaks at 781.5 and 797.9 eV for Co $2p_{3/2}$ and Co $2p_{1/2}$ are attributed to the Co^{2+} spin–orbits. The corresponding satellite peaks can be observed at 803.5 eV (Co $2p_{1/2}$) and 787.1 eV (Co $2p_{3/2}$).[38] In the Ni 2p XPS spectrum (Fig. 3E), strong peaks at 856.02 and 874.06 eV for Ni $2p_{3/2}$ and Ni $2p_{1/2}$ are detected, signifying the presence of Ni^{3+}. The corresponding satellite heights can be observed at 862.24 eV (Ni $2p_{3/2}$) and 880.23 eV (Ni $2p_{1/2}$).[35] In the S 2p XPS spectrum (Fig. 3F), the BEs at 162 and 164.6 eV are attributed to S $2p_{3/2}$ and S $2p_{1/2}$ core levels, respectively. The peak at 162.3 eV is typically assigned to the M^{n+}–S bond in $CoNi_2S_4$ material. Additionally, the other peak at 164.6 eV is assigned to the sulfur ions in low coordination, which is commonly reported to S-vacancies in the material matrix. The highest detected at 168.87 eV is attributed to the shakeup satellite.[39,40]

N_2 ads–des isotherm analysis was done to evaluate pore features and surface area of the g-C_3N_4 and $CoNi_2S_4$@g-C_3N_4 adsorbents. The resulting curves displayed distinct ads/des inflexions and hysteresis loops at P/P_0 ranging from ~0.4 to ~0.9, indicating the porosity of the studied adsorbents (Fig. S3A†). The application of the Brunauer–Emmett–Teller (BET) model revealed a specific surface area of 63.18 $m^2\ g^{-1}$ for g-C_3N_4, which decreased to 8.95 $m^2\ g^{-1}$ for the $CoNi_2S_4$@g-C_3N_4 sample due to the incorporation of $CoNi_2S_4$ within and around the pores. This incorporation process also resulted in a reduction of pore volume from 0.21 $cm^3\ g^{-1}$ (for g-C_3N_4) to 0.033 $cm^3\ g^{-1}$ (for $CoNi_2S_4$@g-C_3N_4). Further analysis using the Barrett–Joyner–Halenda (BJH) method elucidated the distribution of pore sizes in the adsorbents, with narrow peaks observed at 3.02 nm and 2.89 nm, confirming the mesoporous nature of both g-C_3N_4 and $CoNi_2S_4$@g-C_3N_4 adsorbents (Fig. S3B†). These mesoporous characteristics are advantageous for efficiently trapping Au(III) ions.

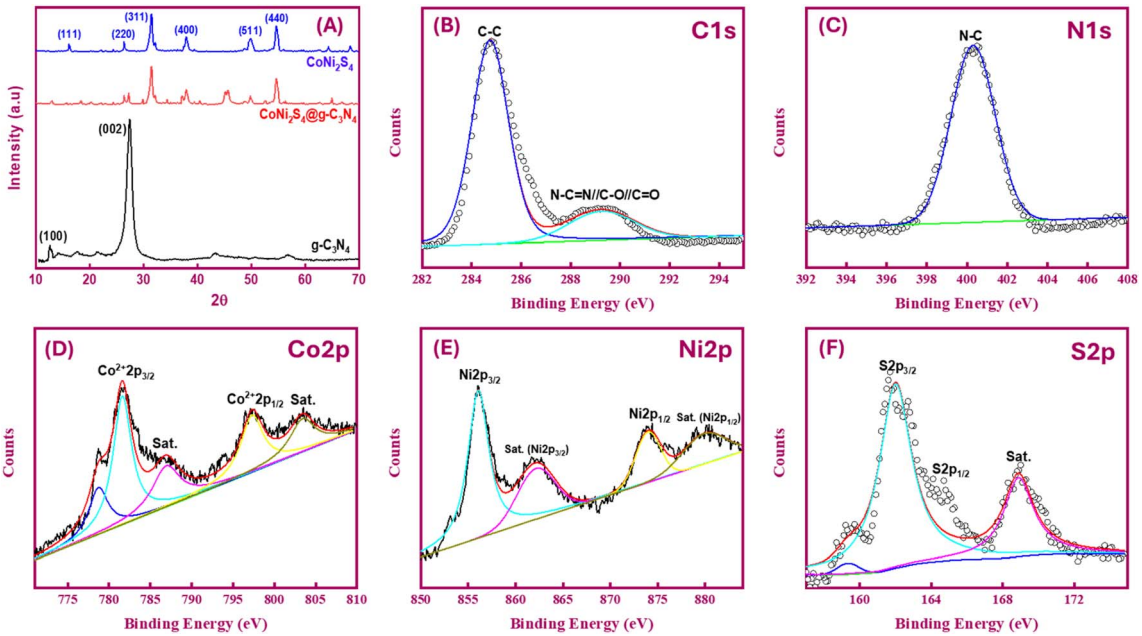

Fig. 3 (A) XRD profiles of g-C_3N_4, $CoNi_2S_4$, and $CoNi_2S_4$@g-C_3N_4; XPS spectra of C 1s (B), N 1s (C), Co 2p (D), Ni 2p (E), and S 2p (F) of $CoNi_2S_4$@g-C_3N_4 sample.

3.2. Au(III) adsorption optimization

The pH significantly influenced the Au(III) trapping. Moreover, the selectivity of the adsorbents for Au(III) ions could be controlled by adjusting the pH value. Variations in pH affected the adsorbent active sites' charge, leading to either improved or demoted Au(III)-trapping efficiency. In the bench-top trials, 20 mg of g-C_3N_4 and $CoNi_2S_4$@g-C_3N_4 adsorbents were stirred with 25 mL of 30 ppm Au(III) solution for 60 minutes over a pH range of 1 to 8 at room temperature. Data in Fig. 4A revealed that 75% and 98.5% of Au(III) could be trapped at pH 2.0 using g-C_3N_4 and $CoNi_2S_4$@g-C_3N_4, respectively. The trapping efficiencies of both adsorbents improved faintly as the pH rose from 1 to 2. In an acidic medium (pH 2), Au(III) was present as a negative $AuCl_4^-$ species. The attraction forces between the active sites of g-C_3N_4 and $CoNi_2S_4$@g-C_3N_4 and $AuCl_4^-$ species were mainly induced by the pH environment. At pH 2, the highest positive charge of g-C_3N_4 and $CoNi_2S_4$@g-C_3N_4 adsorbents was observed (+22 mV to +32 mV), indicating surface protonation (Fig. 4B). The high protonation (H^+) at pH 2 boosted the attraction between negatively $AuCl_4^-$ ions and outer positively charged positions, thereby improving adsorption efficiency. As the pH increased, the surfaces of g-C_3N_4 and $CoNi_2S_4$@g-C_3N_4 began to acquire a negative charge, growing the repulsion between the negatively $AuCl_4^-$ species and the negative-charged sites. Additionally, Au(III) may exist as $[AuCl_3OH]^-$ and $[AuCl_2(OH)_2]^-$ species, creating an electrostatic repulsion behaviour between the anionic Au(III) species and the negative-charged centres.[41,42]

Fig. 4B indicated that the zero-charge points (ZCP) of g-C_3N_4 and $CoNi_2S_4$@g-C_3N_4 adsorbents were found to be at pH 3.5 and 5.1, respectively. At pH < pH_{ZCP}, the active sites on the surfaces of g-C_3N_4 and $CoNi_2S_4$@g-C_3N_4 become positive-charged sites due to the creation of protonated functional groups. Conversely, at pH > pH_{ZCP}, active sites acquire negative charges because of the creation of negatively charged groups. The zeta-potential data proved the highest Au(III)-trapping efficiency obtained at pH 2. The strong binding interactions at this pH ensured maximum adsorption and selectivity for Au(III) ions. Subsequent studies on the trapping of Au(III) ions were conducted using g-C_3N_4 and $CoNi_2S_4$@g-C_3N_4 under optimal pH conditions (*i.e.*, pH 2).

Different doses of g-C_3N_4 and $CoNi_2S_4$@g-C_3N_4 adsorbents (ranging from 5 to 50 mg) were employed to assess the effect of adsorbent dose on the adsorbent performance toward Au(III)-trapping. As presented in Fig. 4C, the adsorption efficiency of g-C_3N_4 and $CoNi_2S_4$@g-C_3N_4 adsorbents increased with the growth of adsorbents quantity. This increase suggests that the adsorption efficiencies of g-C_3N_4 and $CoNi_2S_4$@g-C_3N_4 are dependent on the availability of active surface sites, and larger quantities of adsorbents provide additional internal and external active sites along the adsorbent surfaces, thereby enhancing efficiency. When the adsorbent quantity was insufficient, the number of interior and exterior surface-active sites was less than what was required for whole trapping. Consequently, 20 mg of g-C_3N_4 and $CoNi_2S_4$@g-C_3N_4 adsorbents were found to be enough and suitable for following adsorption experiments.

3.3. Adsorption isotherm study

A series of bench-top tests were conducted to evaluate the impact of initial Au(III) concentrations (ranging from 0.1 to 250 ppm) on the adsorption capacities of g-C_3N_4, $CoNi_2S_4$, and $CoNi_2S_4$@g-C_3N_4 adsorbents under optimal conditions. As shown in Fig. 5A, the adsorption capacities (q_e, mg g^{-1}) of g-

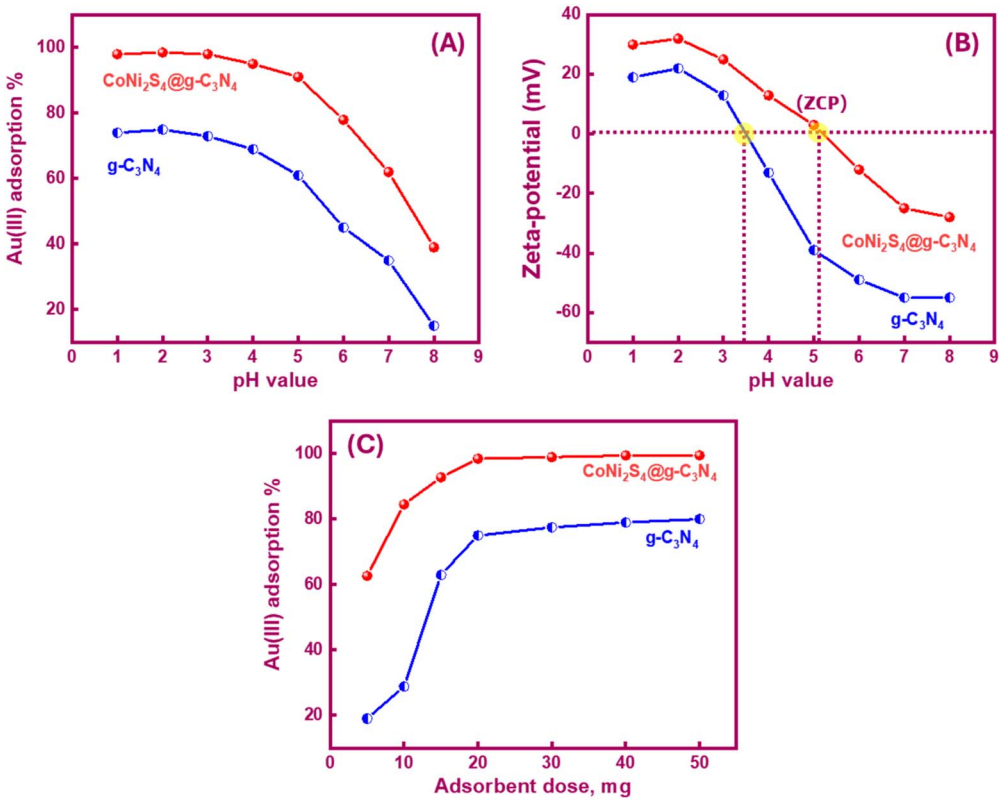

Fig. 4 (A) Impact of pH value on the trapping performance of g-C_3N_4 and $CoNi_2S_4$@g-C_3N_4 adsorbents; (B) zeta-potential profile of g-C_3N_4 and $CoNi_2S_4$@g-C_3N_4 adsorbents based on the change of pH value; (C) effect of −C_3N_4 and $CoNi_2S_4$@g-C_3N_4 dose (mg) on their adsorption performance.

C_3N_4 and $CoNi_2S_4$@g-C_3N_4 increased sharply at low Au(III) concentrations before reaching equilibrium at higher concentrations. This rapid increase at low concentrations is indicative of type I sorption on porous adsorbents, according to the Langmuir classification. The maximum experimental adsorption capacities were found to be 111.25 mg g^{-1} for g-C_3N_4 and 200.6 mg g^{-1} for $CoNi_2S_4$@g-C_3N_4. Fig. S4† presents the Au(III) adsorption capacity of the $CoNi_2S_4$ sample, which was determined to be 132.86 mg g^{-1}. Although this is a significant capacity, it is lower than the 200.6 mg g^{-1} achieved by the $CoNi_2S_4$@g-C_3N_4 nanocomposite. This comparison underscores the enhancement in adsorption performance when $CoNi_2S_4$ is incorporated into the g-C_3N_4 matrix. The g-C_3N_4 support increases the surface area, improves the dispersion of $CoNi_2S_4$ particles, and provides additional active sites for adsorption, collectively boosting the overall adsorption capacity and efficiency. The synergistic interaction between $CoNi_2S_4$ and g-C_3N_4 in the nanocomposite results in superior adsorption kinetics and higher selectivity for Au(III) ions, highlighting the crucial role of the g-C_3N_4 support in the composite material.

Langmuir and Freundlich isotherm models were employed to discover the nature of Au(III)-adsorbents interaction. Additionally, these models were used to determine the theoretical adsorption capacity of g-C_3N_4 and $CoNi_2S_4$@g-C_3N_4 adsorbents, based on the following equations:[43,44]

$$\frac{C_e}{q_e} = \frac{1}{K_L Q_o} + \left(\frac{1}{Q_o}\right) C_e$$

$$R_L = \frac{1}{1 + K_L C_o}$$

$$\ln q_e = \ln K_f + \frac{1}{n} \ln C_e$$

Q_o, K_L and K_f are the theoretical adsorption capacities of g-C_3N_4 and $CoNi_2S_4$@g-C_3N_4 adsorbents (mg g^{-1}), Langmuir constant (L mg^{-1}), and Freundlich constant. And n represents the sorption intensity. The coefficient of determination (R^2) for the linear relationships confirmed that the Langmuir model is more appropriate than the Freundlich model (Fig. 5B and C), indicating the creation of chemical bonds between Au(III) ions and active sites of the g-C_3N_4 and $CoNi_2S_4$@g-C_3N_4 in a single layer. The Q_o, K_L, K_F, and n values were determined and listed in Table 1. The theoretical Q_o values for g-C_3N_4 and $CoNi_2S_4$@g-C_3N_4 adsorbents were 121.95 mg g^{-1} and 205.34 mg g^{-1}, respectively, which aligned well with the experimental results. Additionally, $1/n < 1$ confirmed the chemical interaction between Au(III) ions and used adsorbents. Findings specified

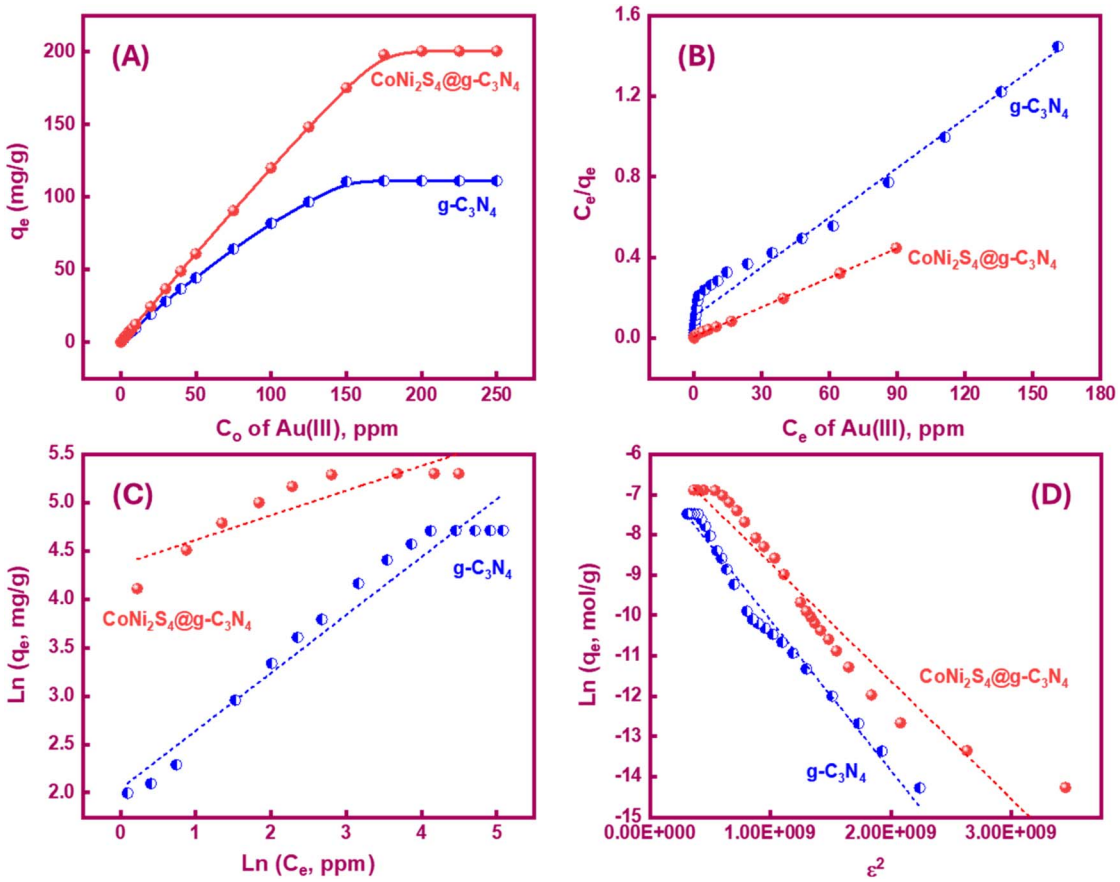

Fig. 5 (A) Effect of preliminary [Au(III)] on the q_e values of g-C_3N_4 and $CoNi_2S_4$@g-C_3N_4 adsorbents, and linear plots of Langmuir (B), Freundlich, and (C) Dubinin–Radushkevich (D–R) (D) isotherm models.

that the g-C_3N_4 and $CoNi_2S_4$@g-C_3N_4 adsorbents are effective at both low and high Au(III) concentration levels.

Furthermore, the Dubinin–Radushkevich (DR) isotherm model characterize of the adsorption process based on the porous structure of g-C_3N_4 and $CoNi_2S_4$@g-C_3N_4 adsorbents:[45,46]

$$\ln q_e = \ln q_o - \delta\varepsilon^2$$

$$\varepsilon = RT \ln\left(1 + \frac{1}{C_e}\right)$$

where ε is the Polanyi potential, C_e (mol L^{-1}) is the equilibrium Au(III)-concentration, q_o (mol g^{-1}) represents the maximum Au(III) adsorption capacity, and δ (mol^2 J^{-2}) is the constant related to the Au(III)-sorption energy. The Au(III)-sorption energy (E, J mol^{-1}) offers insight into the Au(III)-sorption nature. The value of E can be concluded *via* the subsequent relationship:[47]

Table 1 Isotherm and kinetic parameters of Au(III)-sorption using g-C_3N_4 and $CoNi_2S_4$@g-C_3N_4

	Langmuir model		Freundlich model		DR		PFO		PSO		IPD	
g-C_3N_4	Experiential q_m (mg g^{-1})	111.25			R^2	0.97						
	R^2	0.97	R^2	0.95	q_o mol g^{-1}	0.0017	R^2	0.65	R^2	0.98	R^2	0.654
	Q_o	121.95	K_F, mg g^{-1}	7.69	δ mol^2 J^{-2}	3.7×10^{-9}	q_e, mg g^{-1}	100.69	q_e, mg g^{-1}	32.5	I	12.65
	K_L, L mg^{-1}	0.076	n	1.66	E J mol^{-1}	11 624.76	K_1, min^{-1}	0.0033	K_2, g mg^{-1} min^{-1}	0.00313	K_{id} mg g^{-1} $min^{-0.5}$	2.02
					E kJ mol^{-1}	11.624						
$CoNi_2S_4$@g-C_3N_4	Experiential q_m (mg g^{-1})	200.6			R^2	0.93						
	R^2	0.998	R^2	0.77	q_o mol g^{-1}	0.0031	R^2	0.45	R^2	0.999	R^2	0.64
	Q_o	205.34	K_F, mg g^{-1}	77.47	δ mol^2 J^{-2}	2.92×10^{-9}	q_e, mg g^{-1}	181.97	q_e, mg g^{-1}	38.46	I	30.6
	K_L, L mg^{-1}	0.611	n	3.85	E J mol^{-1}	13 085.6	K_1, min^{-1}	0.0019	K_2, g mg^{-1} min^{-1}	0.0124	K_{id} mg g^{-1} $min^{-0.5}$	0.843
					E kJ mol^{-1}	13.085						

$$E = \frac{1}{\sqrt{2\delta}}$$

If the E value is <8 kJ mol^{-1}, the sorbate–sorbent interaction is classified as physisorption, while E value ranging from 8 to 16 kJ mol^{-1} signifies a chemisorption process. In the current study, the E values for g-C_3N_4 and $CoNi_2S_4$@g-C_3N_4 sorbents were estimated as 11.624 and 13.085 kJ mol^{-1}, confirming the chemical nature of the Au(III) adsorption process (Fig. 5D and Table 1).

3.4. Kinetic study of Au(III) adsorption

Determining the required time for the Au(III)-trapping process is economically important to achieve maximum adsorption efficiency within the lowest consumed time as much as possible. So, numerous stirring times (2.5–90 minutes) were tested to explore the impact of stirring time on Au(III)-sorption efficiency. Outcomes in Fig. 6A specified that the Au(III)-trapping efficiency encouraged with longer stirring times, reaching 75% and 98.5% for g-C_3N_4 and $CoNi_2S_4$@g-C_3N_4, respectively, within 60 minutes. Thus, equilibrium could be achieved within 60 minutes. Pseudo-first/second-order (PFO & PSO) kinetic models were employed to investigate the sorption interaction mechanism. The PFO and PSO kinetic equations are described as follows:[48]

$$\log(q_e - q_t) = \log q_e - \left(\frac{K_1}{2.303}\right)t$$

$$\frac{t}{q_t} = \frac{1}{K_2 q_e^{\,2}} + \left(\frac{1}{q_e}\right)t$$

K_1 (min^{-1}) and K_2 (g mg^{-1} min^{-1}) are the rate constants of PFO and PSO models. q_e and q_t represent the quantity of trapped Au(III) ions (mg g^{-1}) at equilibrium and at time t. The constants can be determined from the slope and intercept of the linear plots of $\log(q_e - q_t)$ and t/q_t against t (Fig. 6B and C). The results indicated that the PSO model was more appropriate for illustrating the kinetic pathway of Au(III) adsorption onto g-C_3N_4 and $CoNi_2S_4$@g-C_3N_4, suggesting a chemisorption mechanism. The K_2 value for the $CoNi_2S_4$@g-C_3N_4 adsorbent (0.0124) was greater than that of the g-C_3N_4 adsorbent (0.00313) (Table 1), indicating that $CoNi_2S_4$@g-C_3N_4 has a significantly higher adsorption rate for Au(III) ions. This implies that the composite material $CoNi_2S_4$@g-C_3N_4 enhances the adsorption kinetics, likely due to improved surface properties, increased active sites, or better interaction between sorbents and Au(III) ions.

The Au(III)-sorption process typically progresses through multiple stages, including adsorbate transfer, external prevalence, intra-particle diffusion (IPD), and eventually chemical or

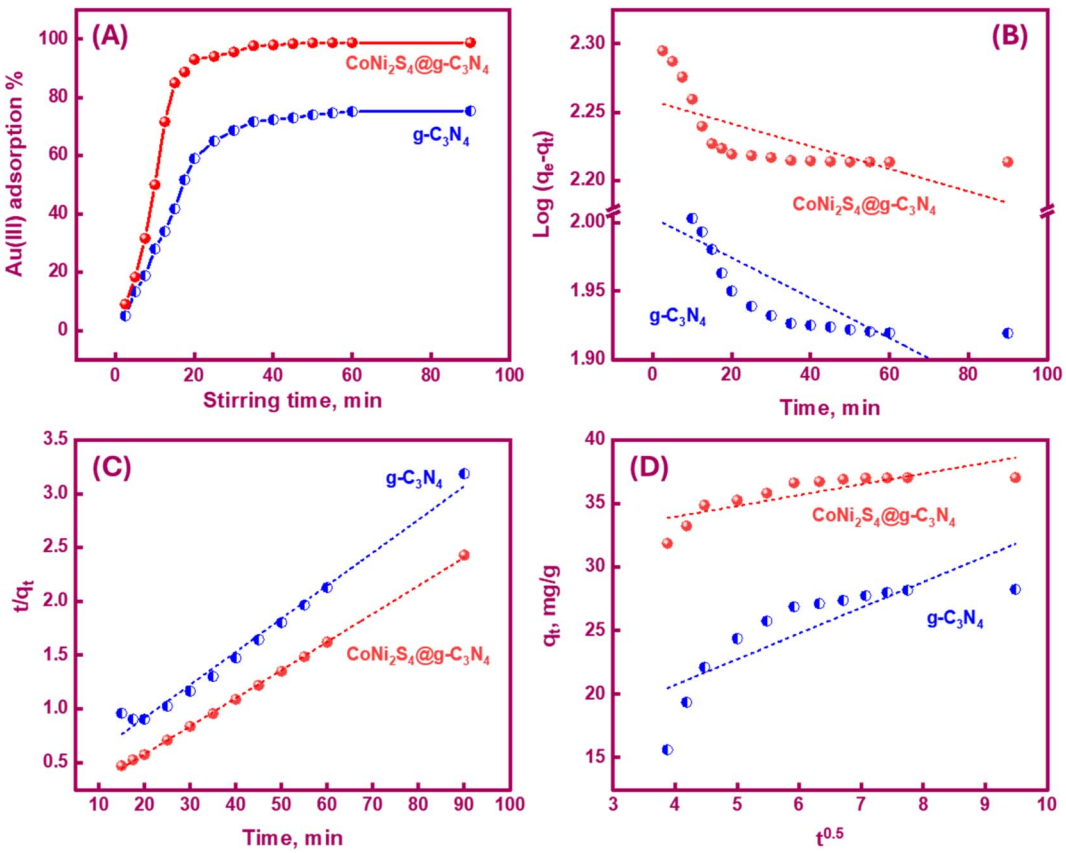

Fig. 6 Effect of stirring time on the trapping efficiency of Au(III) adsorption using g-C_3N_4 and $CoNi_2S_4$@g-C_3N_4 adsorbents, and linear plots of PFO (B), PSO (C), and intra-particle diffusion (D) kinetic models under the best trapping conditions.

physical interaction between the sorbents' active sites and Au(III) ions. The IPD model assumes that the prevalence of Au(III) is the rate-controlling step during the adsorption procedure, and the diffusion direction can vary. This kinetic model was used to evaluate the IPD rate constant. The IPD equation can be represented as next:[49]

$$q_t = K_{id} t^{0.5} + I$$

K_{id} (mg g^{-1} $min^{-0.5}$) is the rate constant of the IPD. The intercept I of the IPD equation depends on the thickness of the external boundary layer. The plot of q_t *versus* $t^{0.5}$ for g-C_3N_4 and $CoNi_2S_4$@g-C_3N_4 adsorbents is shown in Fig. 6D. Table 1 shows the calculated values of R^2, K_{id}, and I. For $CoNi_2S_4$@g-C_3N_4, the K_{id} value is lower than that for g-C_3N_4, suggesting that the diffusion of Au(III) along $CoNi_2S_4$@g-C_3N_4 matrix is slower than g-C_3N_4. This may be due to the dense grafting of $CoNi_2S_4$ along the g-C_3N_4 surface and pores, facilitating quick access to active sites. A higher I value enhances the influence of the outer surface prevalence, improving the rate of the Au(III)-sorption process. Rapid sorption of Au(III) ions using g-C_3N_4 and $CoNi_2S_4$@g-C_3N_4 adsorbents occurred within the first 60 minutes, primarily due to the prevalence of the external layer or mesopores.

3.5. Selectivity study of used adsorbents

Selectivity is a critical factor in metal extraction processes, as it aims to isolate specific ions in their pure states from complex mixtures containing various ions. Here, we investigated the impact of competing ions on the Au(III)-trapping efficiency in both single and combined systems. At the optimal pH of 2, 20 mg of g-C_3N_4 and $CoNi_2S_4$@g-C_3N_4 were stirred with 25 mL of a 30 ppm Au(III) solution, along with 30 ppm of Na(I), K(I), Ag(I), Mg(II), Ca(II), Pd(II), Mn(II), Fe(III), Cu(II), Ni(II), and Al(III). As shown in Fig. 7A, the adsorbents demonstrated a high selectivity for Au(III), with minimal adsorption of other cations. The solution's pH was a significant determinant of this selectivity. In acidic conditions, the high concentration of H^+ ions hindered the adsorption of other cations. Furthermore, when Au(III) was presented alongside another metal ion in binary systems and exposed to the adsorbents at pH 2, findings indicated that competing cations had a negligible impact on Au(III) ions sorption (Fig. 7B).

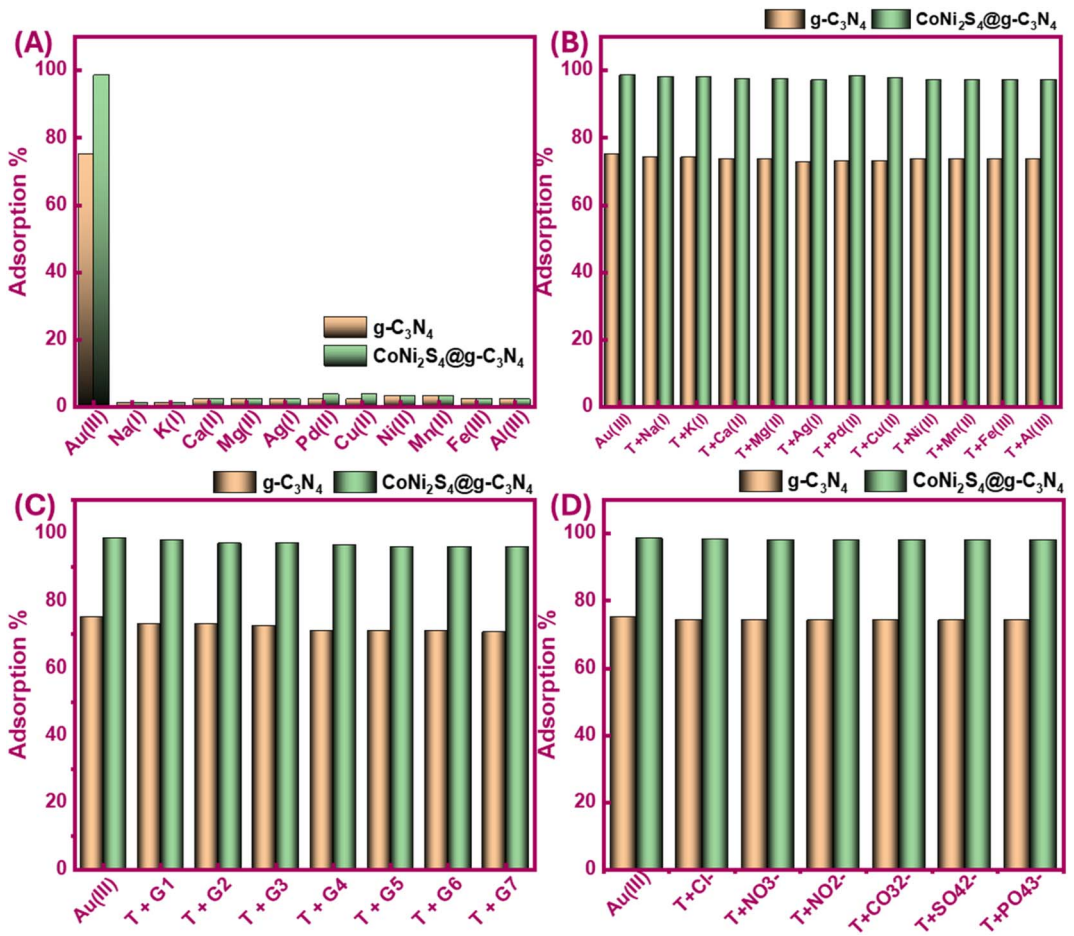

Fig. 7 Selectivity profile of g-C_3N_4 and $CoNi_2S_4$@g-C_3N_4 to adsorb Au(III) ions and other co-existing ions in single (A), binary (B), and group (more than one competitive ion) systems (C), and anions (D) systems at optimum trapping conditions. G1{Au(III) + Ag(I)}, G2{ Au(III) + Cu(II)}, G3{ Au(III) + Mn(II) + Al(III)}, G4{ Au(III) + Co(II) + Hg(II) + Pb(II)}, G5{ Au(III) + Ni(II) Ca(II) + Mn(II) + Fe(III)}, G6{ Au(III) + Al(III) + Mg(II) + Pb(II) + Hg(II) + Cr(III)}, G7{ Au(III) + Hg(II) + Cd(II) + K(I) + Pd(II) + Fe(III)}.

Further batch experiments were conducted in a mixture system using more than one cation with Au(III) (G1 to G7), as explained in Fig. 7C caption. The findings in Fig. 7C demonstrated no noteworthy variation in Au(III) adsorption, maintaining a high adsorption efficiency of 96–98%, despite the presence of increased concentrations of diverse cations. Overall, both g-C_3N_4 and $CoNi_2S_4$@g-C_3N_4 exhibited strong anti-cation interference capabilities, effectively capturing Au(III) with high selectivity. We also evaluated the impact of co-existing anions on the adsorption behavior of Au(III). Fig. 7D shows that the Au(III)-trapping efficiency of g-C_3N_4 and $CoNi_2S_4$@g-C_3N_4 decreased slightly by 1–2% in the company of Cl^-, NO_3^-, NO_2^-, SO_4^{2-}, CO_3^{2-}, and PO_4^{3-} ions. This minor reduction in adsorption efficiency suggests a relatively small adverse impact of these anions on Au(III)-sorption performance. Despite this minor interference, the robust binding between negatively Au(III) species and positive-charged sites of g-C_3N_4 and $CoNi_2S_4$@g-C_3N_4 at pH 2 remained dominant.

3.6. Recycling and reusability of spent extractors

Spent g-C_3N_4 and $CoNi_2S_4$@g-C_3N_4 adsorbents can be recycled using a batch elution/desorption protocol, minimizing the cost of the extraction process and the generated further waste. Elution is essential for obtaining target ions in their pure forms. In bench-top trials, Au(III)-loaded adsorbents were treated with NaOH and thiourea (0.1 M) under continuous stirring to investigate the effect of elution time (Fig. 8A). Thiourea forms a stable complex with Au(III) ions $\{[Au(CS(NH_2)_2)_2]^+\}$in the presence of NaOH, facilitating the desorption of gold from the adsorbent. NaOH adjusts the pH and provides an alkaline environment that enhances the desorption efficiency of the thiourea complex. Results showed that over 99% of the loaded Au(III) were recovered within 60 minutes. The treated g-C_3N_4 and $CoNi_2S_4$@g-C_3N_4 adsorbents were then filtered, dried, and reused for subsequent Au(III) adsorption. Fig. 8B explains that the recycled g-C_3N_4 and $CoNi_2S_4$@g-C_3N_4 adsorbents could be reused for ten cycles. After the tenth cycle, the adsorption efficiency of g-C_3N_4 and $CoNi_2S_4$@g-C_3N_4 adsorbents decreased to 55% and 85%, respectively, while the elution efficacy stayed high (>99%). Despite the decrease in adsorption efficiency due to the stripping agent's adverse effects during repeated operations, which may destroy some of the surface-active sites. The findings indicate that the $CoNi_2S_4$@g-C_3N_4 adsorbent is effective in e-waste treatment and Au(III) ion recovery. This is attributed to its superior efficacy, cost-efficiency, reusability, and robustness even after multiple reuse cycles.

3.7. Au(III) extraction from SMB

Recycling e-waste has garnered global attention as a sustainable strategy for accessing precious metals like gold while mitigating environmental impact. Our study focuses on e-waste recycling using highly selective extractors through a straightforward, rapid, and efficient approach. In this investigation, we utilized mesoporous $CoNi_2S_4$@g-C_3N_4 adsorbent to selectively capture Au(III) ions amidst competitive ions from actual leachate. The extraction of Au(III) from SMB comprised multiple phases: (i) leaching step to release Au(III) ions from SMB to solutions, (ii) adsorption step to adsorb Au(III) ions using $CoNi_2S_4$@g-C_3N_4 adsorbent under the optimum adsorption conditions, and (iii) elution step to collect Au(III) ions in a pure form.

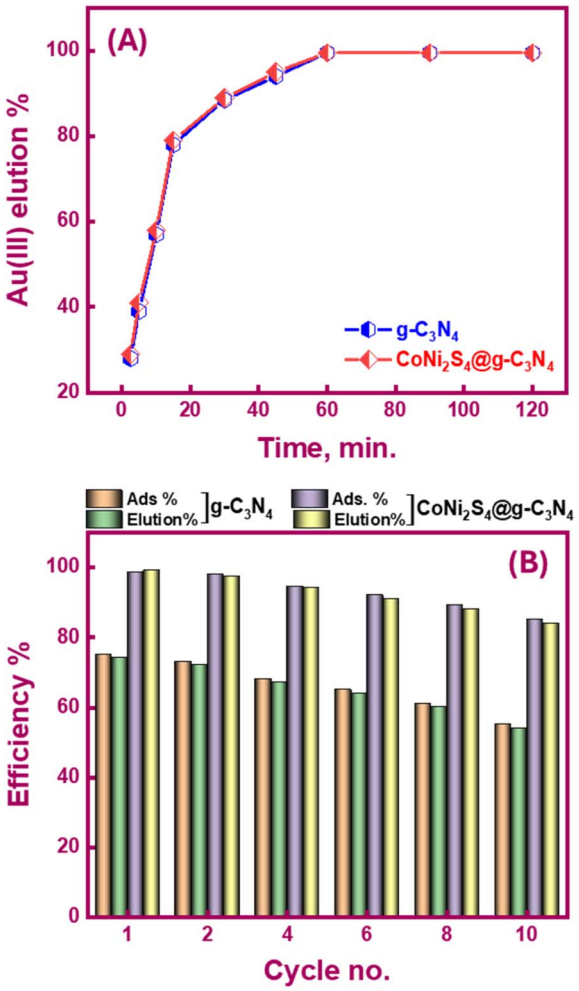

Fig. 8 (A) Influence of stirring time on the elution efficacy of Au(III) ions from used g-C_3N_4 and $CoNi_2S_4$@g-C_3N_4 adsorbents; (B) reusability of g-C_3N_4 and $CoNi_2S_4$@g-C_3N_4 adsorbents under the optimum adsorption and elution circumstances.

The leaching process for Au(III) ion releasing from SMB can be performed using a hydrometallurgical approach, which could be done through the next steps (see Fig. 9):

(i) Gathering SMBs: SMBs were isolated from obsolete computers and crushed into tiny fragments to ease the leaching process.

(ii) Leaching SMBs: Here, 100 g of crushed SMB was stirred overnight with a mixture of H_2SO_4 (5 M) and H_2O_2 (30%) to leach metals such as Ni(II), Fe(III), Al(III), Zn(II), and Cu(II) ions. The remaining solid components were then filtered and separated.

(iii) Dissolving gold ions: The resulting solution was stirred with HNO_3/HCl solution (1 : 3 v : v), leading to a soluble solution of Au(III) ions and other ions.

(iv) Precipitation of other ions: Fe(III), Sn(IV), and Al(III) ions were precipitated using NaOH by adjusting the pH to 4–4.5,

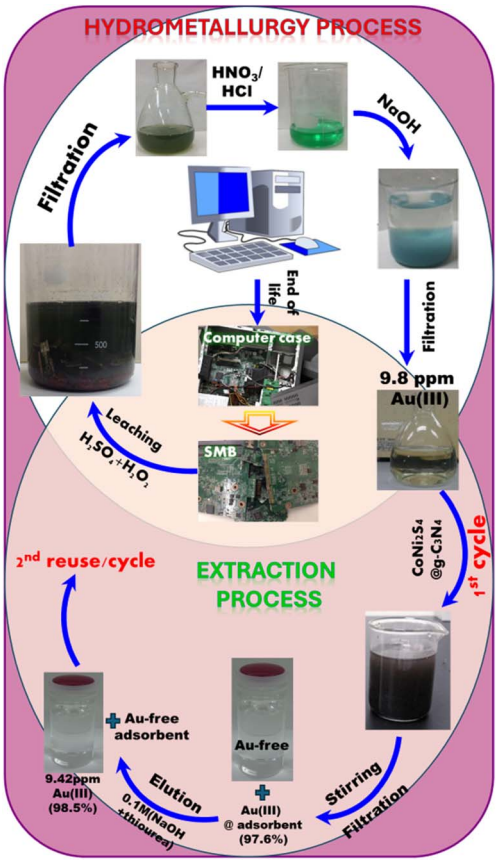

Fig. 9 SMB hydrometallurgical processing and extraction process scheme of the Au(III) ions from the SMBs using mesoporous $CoNi_2S_4$@g-C_3N_4 adsorbent.

while Ag(I) ions were separated using NaCl as AgCl. Precipitates were then eliminated through centrifuge filtration.

(v) The obtained clear solution was employed for selective trapping of Au(III) ions using the $CoNi_2S_4$@g-C_3N_4 adsorbent.

As shown in Table 2, Au(III) ions and other competitive ions concentrations in the resulting liquor were quantified using Atomic Absorption Spectroscopy before interaction with the $CoNi_2S_4$@g-C_3N_4 adsorbent. The $CoNi_2S_4$@g-C_3N_4 adsorbent achieved an adsorption efficiency of 97.6%, and the elution efficiency for these adsorbents was 98.5%. This study demonstrates that the developed $CoNi_2S_4$@g-C_3N_4 adsorbent is highly effective in extracting, recovering, and purifying Au(III) from obsolete SMB. These findings suggest the potential application of $CoNi_2S_4$@g-C_3N_4 adsorbents in environmental cleanup and e-waste management, offering a sustainable solution for recovering valuable Au(III) ions from e-waste sources selectively.

3.8. Advantages and potential limitations of the proposed method

In this section, we comprehensively compare our proposed method for Au(III) extraction using the $CoNi_2S_4$@g-C_3N_4 nanocomposite with other established techniques, highlighting the specific advantages and potential limitations.

(I) Leaching process: pyrometallurgy involves high-temperature processing, which can efficiently extract gold and other metals from e-waste. However, these methods often require significant energy input, generate toxic by-products, and have lower selectivity, contaminating the recovered metals. In contrast, hydrometallurgy uses aqueous solutions to leach metals, which can be more environmentally friendly than pyrometallurgical methods. Therefore, we followed the hydrometallurgy method in the leaching process.

(II) Adsorption process: the $CoNi_2S_4$@g-C_3N_4 nanocomposite demonstrates a high adsorption capacity of 200.6 mg g^{-1}, rapid adsorption kinetics, and excellent reusability, maintaining over 85% efficiency after ten cycles. These features make it a superior adsorbent compared to many conventional materials, as shown in Table 3. Table 3 compares the adsorption capacities of various adsorbents for extracting Au(III) ions from aqueous solutions. The results demonstrate that $CoNi_2S_4$@g-C_3N_4 excels in Au(III) adsorption, surpassing the performance of several other materials. These findings suggest that the $CoNi_2S_4$@g-C_3N_4 nanocomposite holds considerable promise for selectively capturing Au(III) ions from e-waste.

(III) Specific advantages of our proposed method: (i) the $CoNi_2S_4$@g-C_3N_4 nanocomposite shows exceptional selectivity for Au(III) ions, even in the presence of competing metal ions, and a high adsorption capacity, outperforming many traditional adsorbents; (ii) the process operates under mild conditions, reducing energy requirements and minimizing the use of hazardous chemicals. The reusability of the adsorbent further reduces operational costs and environmental impact; (iii) our method has been tested with actual e-waste leachates, demonstrating its effectiveness in real-world scenarios. The results indicate that the method can be easily scaled up for industrial applications, providing a viable solution for sustainable gold recovery.

(IV) Potential limitations: (i) using Co and Ni in the nanocomposite raises concerns about the sustainability and availability of these critical minerals. However, the high reusability and potential for recycling these materials mitigate this concern to some extent; (ii) while the adsorbent can be reused, the regeneration process must be optimized to ensure minimal loss of adsorption capacity and material integrity over multiple cycles.

Table 2 Selective adsorption study of Au(III) ions using $CoNi_2S_4$@g-C_3N_4 adsorbent at specific extraction/elution conditions

[Coexisted metal ions] (ppm)	[Au(III)] (ppm)	[Au(III)], after adsorption (ppm)	[Au(III)], after elution (ppm)	Adsorption %	Elution %
Ag(I) 0.06, Pd(II) 0.12, Cu(II) 5.25, Ni(II) 1.7, Mn(II) 0.07, Fe(III) 9.3, Al(III) 10.8, Zn(II) 3.85, Pb(II) 0.03, Hg(II) 0.02, Cd(II) 0.02	9.8	0.235	9.42	97.6	98.5

Table 3 Comparing adsorption capacity for different materials that adsorb Au(III) ions

Adsorbents	Adsorption capacity mg g^{-1}	Ref.
g-C_3N_4	111.25	Here
$CoNi_2S_4$@g-C_3N_4	200.6	
Zr-MOF functionalized with mercapto-1,3,4-thiodiazole	301.5	50
UiO-66-NH_2 modified by amidinothiourea	227.68	51
Dowex Marathon MSA commercial resin	73.53	52
Cellulose-based bio-adsorbent	5.07 mmol g^{-1}	53
Humic acid	182.82	54
N-(2-[bis(2-aminoethyl)amino)ethyl]aminomethyl-polystyrene polymer bead	173.18	55
Imprinted ionic material SiO_2(BGS/RHA)-TMPDT-Im-Au)	10.44	56
Ureido polymers containing large repeating ring	37.6	57
Clay mineral composite	108.3	58
Functionalized silica coating mercapto on iron sand magnetic material	125	59

4. Conclusion

In this study, we successfully synthesized a hybrid mesoporous nanocomposite of $CoNi_2S_4$@g-C_3N_4 for the selective recovery of Au(III) ions from SMB. The $CoNi_2S_4$@g-C_3N_4 nanocomposite achieved a remarkable adsorption capacity of 200.6 mg g^{-1} at pH 2, significantly better than that of g-C_3N_4 alone (111.25 mg g^{-1}). The high selectivity for Au(III) ions over other competitive ions in both single and multi-ion systems underscores the potential of $CoNi_2S_4$@g-C_3N_4 as an effective adsorbent for gold recovery from e-waste. The adsorption process reached equilibrium within 60 minutes, fitting well with the PSO kinetic model. This rapid adsorption rate is advantageous for practical applications, where time efficiency is critical. The $CoNi_2S_4$@g-C_3N_4 nanocomposite exhibited excellent reusability, maintaining high adsorption efficiency (>85%) after ten cycles of adsorption and desorption. This recyclability, combined with the ease of synthesis, makes $CoNi_2S_4$@g-C_3N_4 a cost-effective and sustainable solution for industrial-scale gold recovery. In practical applications, the $CoNi_2S_4$@g-C_3N_4 nanocomposite demonstrated high efficiency in extracting Au(III) ions from the leach liquor of SMB. The adsorption efficiency was 97.6%, with an elution efficiency of 98.5%, highlighting the nanocomposite's practical utility in e-waste management and resource recovery. In conclusion, the $CoNi_2S_4$@g-C_3N_4 nanocomposite presents a promising and viable adsorbent for the choosy recovery of Au(III) from e-waste. Its high adsorption capacity, rapid kinetics, excellent selectivity, and reusability make it an attractive candidate for sustainable gold recovery processes. Future studies could focus on scaling up the synthesis process and exploring the application of $CoNi_2S_4$@g-C_3N_4 for recovering other valuable metals from various types of e-waste.

Data availability

Relevant data are included in the paper and its ESI files.† Other data and parameters generated or analyzed during the study are available from the corresponding author upon reasonable request.

Conflicts of interest

There are no conflicts to declare.

Acknowledgements

This paper is based upon work supported by the Science, Technology & Innovation Funding Authority (STDF) under grant number 45936.

References

1 M. Peydayesh, E. Boschi, F. Donat and R. Mezzenga, *Adv. Mater.*, 2024, **36**, 2310642.
2 C. Khaobang, N. Kathongthung, P. Phitsuwan, P. Sitthichirachat, H. Wibowo and C. Areeprasert, *J. Anal. Appl. Pyrolysis*, 2024, **179**, 106465.
3 K. Liu, Q. Tan, J. Yu and M. Wang, *Circ. Econ.*, 2023, **2**, 100028.
4 X. Liu, R. Liu, Y. Lu, Q. Sun, W. Xue, M. Cheng and Y. Yang, *Sep. Purif. Technol.*, 2024, **328**, 125049.
5 Y.-R. Chen, X.-Y. Fan, H.-F. Wei, L. Liao, Y. Hu, Y. Lu, X. Wang, Y. Li and W.-R. Cui, *Sep. Purif. Technol.*, 2024, **347**, 127521.
6 V. Rahimi, E. A. Inzulza-Moraga, D. Gómez-Díaz, M. S. Freire and J. González-Álvarez, *Environ. Sci. Pollut. Res.*, 2024, 1–16, DOI: 10.1007/s11356-024-32793-1.
7 B. C. Choudhary, D. Paul, A. U. Borse and D. J. Garole, *Sep. Purif. Technol.*, 2018, **195**, 260–270.
8 Z. Qian, X. Chen, X. Zhang, P. Kang, H. Huang, Q. Lan, Q.-Z. Zhong, Y. Lv, X. Ling and T. Liu, *Chem. Eng. J.*, 2024, **490**, 151884.
9 R. Fan, F. Xie, X. Guan, Q. Zhang and Z. Luo, *Bioresour. Technol.*, 2014, **163**, 167–171.
10 S. Saha, H. Basu, S. Singh and R. Kumar Singhal, *J. Environ. Manage.*, 2024, **363**, 121384.
11 M. D. Rao, K. K. Singh, C. A. Morrison and J. B. Love, *Sep. Purif. Technol.*, 2021, **263**, 118400.
12 M. M. Selim, A. Tounsi, H. Gomaa, N. Hu and M. Shenashen, *Alex. Eng. J.*, 2024, **100**, 61–71.

13 T. S. Nguyen, Y. Hong, N. A. Dogan and C. T. Yavuz, *Chem. Mater.*, 2020, **32**, 5343–5349.
14 T. H. Bui, S. Jeon and Y. Lee, *J. Environ. Chem. Eng.*, 2021, **9**, 104661.
15 H. Gomaa, M. A. Shenashen, A. Elbaz, S. Kawada, T. A. Seaf El-Nasr, M. F. Cheira, A. I. Eid and S. A. El-Safty, *J. Colloid Interface Sci.*, 2021, **604**, 61–79.
16 Y.-C. Lo, C.-L. Cheng, Y.-L. Han, B.-Y. Chen and J.-S. Chang, *Bioresour. Technol.*, 2014, **160**, 182–190.
17 M. M. Selim, A. Tounsi, H. Gomaa and M. Shenashen, *AIP Adv.*, 2024, **14**, 40703.
18 L. Zhang, Q.-Q. Zheng, S.-J. Xiao, J.-Q. Chen, W. Jiang, W.-R. Cui, G.-P. Yang, R.-P. Liang and J.-D. Qiu, *Chem. Eng. J.*, 2021, **426**, 131865.
19 H. A. Abdelmonem, T. F. Hassanein, H. E. Sharafeldin, H. Gomaa, A. S. A. Ahmed, A. M. Abdel-lateef, E. M. Allam, M. F. Cheira, M. E. Eissa and A. H. Tilp, *Colloids Surf. A Physicochem. Eng. Asp.*, 2024, **684**, 133081.
20 W. Zhou, H. Liang, Y. Lu, H. Xu and Y. Jiao, *Waste Manage.*, 2021, **120**, 530–537.
21 J. Liu, Z. Deng, H. Yu and L. Wang, *Chem. Eng. J.*, 2021, **410**, 128360.
22 Z. Chen, S. Zhang, Y. Liu, N. S. Alharbi, S. O. Rabah, S. Wang and X. Wang, *Sci. Total Environ.*, 2020, **731**, 139054.
23 H. Xie, J. Zhang, D. Wang, J. Liu, L. Wang and H. Xiao, *Appl. Surf. Sci.*, 2020, **504**, 144456.
24 S. Guo, N. Duan, Z. Dan, G. Chen, F. Shi and W. Gao, *J. Mol. Liq.*, 2018, **258**, 225–234.
25 A. Modwi, O. Aldaghri, K. H. Ibnaouf, K. K. Taha and M. Bououdina, *J. Water Proc. Eng.*, 2024, **59**, 104956.
26 A. Chowdhury, S. Kumari, A. A. Khan and S. Hussain, *J. Environ. Chem. Eng.*, 2021, **9**, 106554.
27 V. Kromah and G. Zhang, *Water*, 2021, **13**, 1843.
28 A. Chowdhury, B. Mahto, S. Kumari, A. A. Khan and S. Hussain, *J. Environ. Chem. Eng.*, 2023, **11**, 109199.
29 M. Sajid, A. Sharma, A. Choudhry and S. A. Chaudhry, *Colloids Surf., C*, 2023, **1**, 100011.
30 F. Liu, S. Wang, Z. Hu and B. Hu, *Sep. Purif. Technol.*, 2024, **329**, 125218.
31 H. Gomaa, C. An, Q. Deng, H. A. Altaleb, S. M. Gomha, T. Z. Abolibda, M. A. Shenashen and N. Hu, *J. Ind. Eng. Chem.*, 2024, DOI: **10.1016/j.jiec.2024.06.023**.
32 H. Gomaa, M. A. Shenashen, M. F. Cheira, K. Sueki, T. A. Seaf El-Nasr, M. M. Selim and S. A. El-Safty, *J. Clean. Prod.*, 2023, **402**, 136819.
33 H. Gomaa, M. Y. Emran, M. M. Elsenety, R. D. Abdel-Rahim, Q. Deng, M. I. Gadallah, M. Saad, H. ALMohiy, M. Ezzeldien, T. A. Seaf El-Nasr, M. S. A. El-Gaby and A. M. Aboraia, *ACS Sustain. Chem. Eng.*, 2023, **11**, 2127–2138.
34 L. Ge, *Mater. Lett.*, 2011, **65**, 2652–2654.
35 J. Zhu, C. Han and X. Song, *Mater. Chem. Phys.*, 2022, **283**, 126038.
36 S. Fang, Y. Xia, K. Lv, Q. Li, J. Sun and M. Li, *Appl. Catal. B Environ.*, 2016, **185**, 225–232.
37 Y. Li, S. Wu, L. Huang, J. Wang, H. Xu and H. Li, *Mater. Lett.*, 2014, **137**, 281–284.
38 Z. Li, D. Zhao, C. Xu, J. Ning, Y. Zhong, Z. Zhang, Y. Wang and Y. Hu, *Electrochim. Acta*, 2018, **278**, 33–41.
39 Y. Han, S. Sun, W. Cui and J. Deng, *RSC Adv.*, 2020, **10**, 7541–7550.
40 Z. He, H. Wang, M. Liang, H. Ma, C. Zhang, Y. Zhao, Y. Qu and Z. Miao, *Int. J. Hydrogen Energy*, 2024, **49**, 81–89.
41 K. Paclawski, *J. Min. Metall. B Metall.*, 2015, **51**, 133–142.
42 M. Wojnicki, E. Rudnik, M. Luty-Błocho, K. Pacławski and K. Fitzner, *Hydrometallurgy*, 2012, **127–128**, 43–53.
43 S. H. Al-Ansari, H. Gomaa, R. D. Abdel-Rahim, G. A. M. Ali and A. M. Nagiub, *Sci. Rep.*, 2024, **14**, 4379.
44 M. Thabet, E. M. Abd El-Monaem, W. R. Alharbi, M. Mohamoud, A.-H. Abdel-Aty, I. Ibrahim, M. A. Abdel-Lateef, A. E. S. Goda, T. A. Seaf Elnasr, R. Wang and H. Gomaa, *J. Water Proc. Eng.*, 2024, **60**, 105192.
45 A. Rahmani-Sani, A. Hosseini-Bandegharaei, S.-H. Hosseini, K. Kharghani, H. Zarei and A. Rastegar, *J. Hazard Mater.*, 2015, **286**, 152–163.
46 E. A. Abdel-Galil, R. S. Hassan and M. A. Eid, *Appl. Radiat. Isot.*, 2019, **148**, 91–101.
47 H. Gomaa, M. A. Shenashen, M. F. Cheira, K. Sueki, T. A. Seaf El-Nasr, M. M. Selim and S. A. El-Safty, *Chem. Eng. J.*, 2023, **461**, 142014.
48 H. Gomaa, M. A. Shenashen, M. F. Cheira, K. Sueki, T. A. Seaf El-Nasr, M. M. Selim and S. A. El-Safty, *J. Clean. Prod.*, 2023, **402**, 136819.
49 H. Gomaa, M. Y. Emran, M. M. Elsenety, R. D. Abdel-Rahim, Q. Deng, M. I. Gadallah, M. Saad, H. ALMohiy, H. R. H. Ali, F. A. Faraghally, T. A. Seaf El-Nasr, M. S. A. El-Gaby and A. M. Aboraia, *J. Water Proc. Eng.*, 2023, **51**, 103436.
50 C. Wang, G. Lin, J. Zhao, S. Wang and L. Zhang, *Chem. Eng. J.*, 2020, **388**, 124221.
51 M. Zhao, Z. Huang, S. Wang, L. Zhang and C. Wang, *Microporous Mesoporous Mater.*, 2020, **294**, 109905.
52 P. K. Patel, S. Nagireddi, R. V. S. Uppaluri and L. M. Pandey, *Mater. Today: Proc.*, 2022, **68**, 824–829.
53 F. B. Biswas, I. M. M. Rahman, K. Nakakubo, M. Endo, K. Nagai, A. S. Mashio, T. Taniguchi, T. Nishimura, K. Maeda and H. Hasegawa, *J. Hazard. Mater.*, 2020, **410**, 124569.
54 H. Niu, H. Yang and L. Tong, *Colloids Surf. A Physicochem. Eng. Asp.*, 2021, **630**, 127442.
55 M. Sayın, M. Can and M. İmamoğlu, *J. Chem. Eng. Data*, 2021, **66**, 1132–1143.
56 S. Hastuti, S. Wahyuningsih, T. Martini and I. N. Hayati, in *IOP Conference Series: Materials Science and Engineering*, IOP Publishing, 2019, vol. 578, p. 12018.
57 Y. Sun, Y. Ding, W. Zhou, X. Wang, C. Tan, Y. Matsumura, B. Ochiai and Q. Chu, *ACS Omega*, 2021, **6**, 28004–28011.
58 Y. Rakhila, A. Elmchaouri, A. Mestari, S. Korili, M. Abouri and A. Gil, *Int. J. Miner. Metall. Mater.*, 2019, **26**, 673–680.
59 M. Karbeka, in *IOP Conference Series: Materials Science and Engineering*, IOP Publishing, 2020, vol. 823, p. 12031.